H_4O^{2+} ion stabilized by pressure

Jingyu Hou,[1,4] Haixu Cui,[2] Artem R. Oganov,[3] Han-Fei Li,[1] Xiao-Ji Weng,[4] Xiang-Feng Zhou,[4] Hui-Tian Wang,[5] and Xiao Dong[1,*]

[1]*Key Laboratory of Weak-Light Nonlinear Photonics, School of Physics, Nankai University, Tianjin 300071, China*
[2]*College of Physics and Materials Science, Tianjin Normal University, Tianjin 300387, China*
[3]*Skolkovo Institute of Science and Technology, Bolshoy Boulevard 30, Building 1, Moscow 121205, Russia*
[4]*Center for High Pressure Science, State Key Laboratory of Metastable Materials Science and Technology, School of Science, Yanshan University, Qinhuangdao 066004, China*
[5]*National Laboratory of Solid-State Microstructures, School of Physics, Collaborative Innovation Center of Advanced Microstructures, Nanjing University, Nanjing 210093, China*

(Received 2 December 2022; revised 27 February 2024; accepted 10 April 2024; published 1 May 2024)

Aquodiium (H_4O^{2+}), an isoelectronic analog of the ammonium ion (NH_4^+), can theoretically be formed by combining a molecule of water (H_2O) with two protons. However, stable aquodiium has never been reported because of the high energy cost during the second protonation after hydronium (H_3O^+). Here, by performing *ab initio* evolutionary structure searches combined with first-principles calculations, stable ionic phases, H_4OF_2 and $H_4OF_2 \cdot HF$, were predicted to be thermodynamically stable at high pressure. Analysis of bond lengths and electron density supports the formation of aquodiium under pressure in these two phases. Moreover, *ab initio* molecular dynamics simulations reveal that these ionic phases will enter the superionic states at lower temperatures compared to water ice. For $H_4OF_2 \cdot HF$, there is a plastic phase region where aquodiium ions exhibit free rotation. All aquodiium ions are fully preserved below 1000 K in these ionic phases, while after entering the diffusion state, only the H_4OF_2 phase keeps H_4O^{2+} ions. Our results suggest that pressure stabilizes the H_4O^{2+} ion, presenting an important addition to traditional physical and chemical theories such as the valence shell electron pair repulsion model, proton transfer, and acid-base theory.

DOI: 10.1103/PhysRevB.109.174102

I. INTRODUCTION

H_3O^+ (hydronium), the unique ion produced from water ionization, is essential to maintain the acid-base balance of water and plays a decisive role in many important physical, chemical, and biochemical processes. Actually, H_3O^+ has a lone electron pair on the O atom, which could attract an additional proton to form H_4O^{2+}, which is isoelectronic with methane (CH_4) and ammonium ion (NH_4^+) and has the same sp^3 hybridization. Here we call the H_4O^{2+} ion aquodiium by comparison with ammonium and hydronium ions. It was first proposed that aquodiium might be present in some gaseous excited ions or might exist as a transition state during hydrogen-deuterium transfer [1,2]. However, no neutral stable compounds containing aquodiium have been found, and the closest analog is $[(LAu_4O)]^{2+}$, where L is the donor ligand PAr_3 and Ar denotes aryl [3]. Aquodiium is the missing piece in the picture of the series of tetrahedral molecules and ions $CH_4 \rightarrow NH_3(NH_4^+) \rightarrow H_2O(H_3O^+, H_4O^{2+})$, so elegantly described by the valence shell electron pair repulsion (VSEPR) model [4]. Due to the strong repulsion between hydronium (H_3O^+) and H^+, both of which have a positive charge, it is difficult to protonate hydronium further. Besides, the small size of the oxygen atom makes the charge more compact, and steric hindrance further destabilizes H_4O^{2+}. Thermodynamically, the affinity of water to two protons can be described by the energy difference $E[H_3O^+] + E[H^+] - E[H_4O^{2+}]$, which is highly negative at -60 kcal/mol, according to theoretical estimates [5,6], implying that aquodiium (H_4O^{2+}) is unlikely to exist under mild conditions.

Pressure proved to be an effective tool for altering the chemistry of the elements and it will trigger a series of reactions that are near unthinkable at ambient pressure, resulting in a series of exotic compounds [7,8], such as novel Na_2Cl and $NaCl_3$ [9], CsF_n ($n > 1$) [10,11], and various noble gas compounds [12–17]. The external pressure may offset the electrostatic repulsion and stabilize H_4O^{2+}, and ice is the simplest system possible to realize this iconic cation. At high pressure, water ice exhibits complex structures and anomalous properties [18–28]. Ice experimentally transforms into phase X, a nonmolecular crystal featuring symmetric hydrogen O-H bonds under pressures above 68 GPa [18,19], and its structure can be viewed as a three-dimensional polymer of H_4O units that share hydrogen atoms. Interestingly, a partially ionic phase (monoclinic $P2_1$ structure) consisting of alternating layers of $(OH)^{\delta-}$ and $(H_3O)^{\delta+}$ ($\delta = 0.62$) in water ice was predicted at zero temperature and pressures above 1400 GPa [28]. The extreme pressure causes one H_2O molecule to grab a proton from another H_2O molecule, completing the first protonation and forming a stable ionic crystal. Yet at such high pressures, there is still no sign of H_4O^{2+}. A favorable

*Corresponding author: xiao.dong@nankai.edu.cn

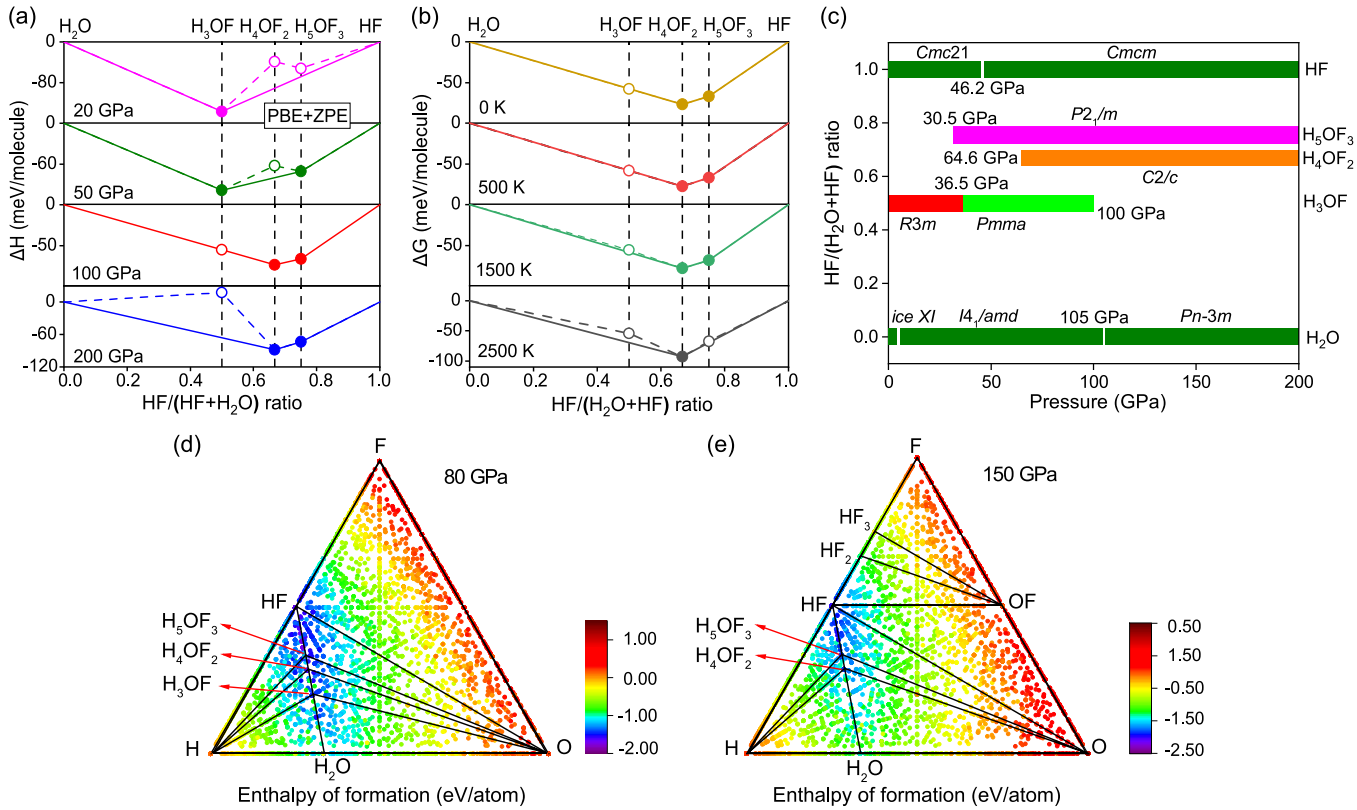

FIG. 1. Thermodynamic stability in the H_2O-HF system. (a) Predicted convex hulls of the H_2O-HF system at high pressures and zero temperature. (b) Predicted Gibbs free energies of H_2O-HF system at 100 GPa as a function of temperature. Stable structures (solid circles) are located on the solid lines and unstable compounds (open circles) are located on the dashed lines. (c) Pressure-composition phase diagram. Zero-point energy (ZPE) was included. Ice XI, ice VIII ($I4_1/acd$), and ice X (Pn-$3m$) for H_2O [18,31,32], as well as the $Cmc2_1$ and $Cmcm$ phases of HF [33,34], were considered to be the stable reactants over the calculated pressure range. Predicted ternary phase diagram and convex hull (black line) based on the enthalpies of formation of compounds in the H-F-O system at (d) 80 GPa and (e) 150 GPa.

condition for forming H_4O^{2+} at a lower cost is to introduce a surplus of H protons; i.e., H_3O^+ may be further protonated in the presence of strong acids under extreme conditions. Here, we report the formation of aquodiium induced by pressure in the H_2O-HF system.

II. RESULTS AND DISCUSSION

Possible stable compounds in the H_2O-HF system were explored using the variable-composition evolutionary algorithm USPEX [29,30] at pressures of 50, 80, 100, 120, 150, 200, and 300 GPa. Here, the enthalpy of formation is defined as $\Delta H = H[(H_2O)_{1-x}(HF)_x] - (1\text{-}x)H(H_2O) - xH(HF)$, and stable compounds should have negative and lower formation enthalpy (ΔH) than any isochemical phases or phase assemblages. Detailed methods are listed in Appendix A. Figure 1 shows the convex hull, Gibbs free energies, and pressure-composition phase diagram. Zero-point energy (ZPE) was also included in the calculation of the enthalpy of formation since this quantum nuclear effect can be important for compounds of light atoms. Several thermodynamically stable stoichiometries, such as H_3OF, H_4OF_2, and H_5OF_3, emerge in the H_2O-HF system at high pressures [Fig. 1(a)]; their lattice parameters and atomic positions are listed in Appendix B (Table I). As shown in Fig. 1(c), water ice and hydrogen fluoride first react at a stoichiometric ratio giving 1:1 of H_3OF at zero pressure and this compound undergoes a transition from the $R3m$ phase to the $Pmma$ phase at 36.5 GPa. As pressure increases, newly predicted compounds, H_4OF_2 and H_5OF_3, become thermodynamically stable at pressures of 64.6 and 30.5 GPa, respectively, and remain stable to at least 200 GPa. In the studied pressure range, each of these two compounds has just one phase, and their symmetries are $C2/c$ and $P2_1/m$, respectively. Remarkably, different compounds may coexist in a wide range of pressures. For example, H_3OF and H_5OF_3 compounds can coexist at pressures from 30.5 to 100 GPa; all three compounds can coexist from 64.6 to 100 GPa; and when pressure exceeds 100 GPa, H_3OF decomposes into H_4OF_2 and H_2O, leaving just H_4OF_2 and H_5OF_3 to coexist.

Since temperature has an important effect on structural stability, we further investigated the effect of temperature using the quasiharmonic approximation. At 100 GPa, H_5OF_3 is unstable with respect to decomposition into H_4OF_2 and HF at temperatures above 2500 K, and high temperature does not destabilize H_4OF_2, which remains a thermodynamically stable phase [Fig. 1(b)] at high pressures and high temperatures. Additionally, considering that the decomposition path of newly predicted compounds may extend beyond H_2O and HF, we investigated their thermodynamic stability in a wider compositional space, i.e., the H-F-O ternary composition space. In the ternary phase diagram, the enthalpies of formation with lower negative

TABLE I. Crystal structures of the thermodynamically stable phases in the H_2O-HF system.

	Pressure (GPa)	Space group	Lattice parameters (Å)	Wyckoff positions (fractional coordinates)
H_3OF	50	$R3m$	$a = b = c = 2.7741$ $\alpha = \beta = \gamma = 87.1578^\circ$	H1: 3b (0.77734, 0.77734, 0.34660) F1: 1a (0.05960, 0.05960, 0.05960) O1: 1a (0.56163, 0.56163, 0.56163)
	100	$Pmma$	$a = 3.6856$ $b = 3.5316$ $c = 2.7235$ $\alpha = \beta = \gamma = 90^\circ$	H1: 4k (0.25000, 0.74895, 0.54072) H2: 2b (0.00000, 0.50000, 0.00000) F1: 2e (0.25000, 0.00000, 0.24764) O1: 2f (0.25000, 0.50000, 0.75528)
H_4OF_2	150	$C2/c$	$a = 3.7019$ $b = 6.8762$ $c = 5.8667$ $\alpha = \gamma = 90^\circ$ $\beta = 141.8172^\circ$	H1: 8f (−0.28438, −0.25802 −0.28141) H2: 8f (0.26510, −0.07143, 0.02142) F1: 4e (0.00000, 0.66273, 0.25000) F2: 4e (0.00000, 0.99335, 0.25000) O1: 4e (0.00000, 0.33604, 0.25000)
H_5OF_3	150	$P2_1/m$	$a = 4.3575$ $b = 3.6129$ $c = 4.3676$ $\alpha = \gamma = 90^\circ$ $\beta = 118.1131^\circ$	H1: 4f (0.23068, 0.98592, 0.53711) H2: 2e (0.65971, 0.25000, 0.08046) H3: 2e (0.59222, 0.75000, 0.71454) H4: 2e (0.94908, 0.25000, 0.87440) F1: 2e (0.15099, 0.25000, 0.33583) F2: 2e (0.65906, 0.25000, 0.82125) F3: 2e (0.83623, 0.75000, 0.15849) O1: 2e (0.34177, 0.75000, 0.67417)

values are still concentrated on the line between H_2O and HF. Among them, H_4OF_2 and H_5OF_3 have strongly negative enthalpies of formation and their thermodynamic stability is protected [Figs. 1(d) and 1(e)]. The electronic structures and lattice dynamics for the new predicted compounds were examined. They all exhibit a wide direct band gap, indicating their insulating character (see Fig. 8 in Appendix B). The absence of any imaginary phonon frequencies in the whole Brillouin zone demonstrates that they are all dynamically stable (see Fig. 9 in Appendix B).

For the compound H_3OF, there are two ionic phases, $R3m$ and $Pmma$, consisting of H_3O^+ ions and F^- ions (see Appendix C). It is noteworthy that the discovery of new stable compounds is concentrated in the HF-rich region, which provides a stable proton-rich environment for the emergence of H_4O^{2+}. High pressure also favors this, because utilization of the lone electron pair of the H_3O^+ ion for bonding with H^+ decreases volume. Figures 2(a) and 2(b) depict the structures of the two phases at 150 GPa. Intriguingly, both feature well-separated F^- and H_4O^{2+} ions at 150 GPa. In H_4OF_2, each O atom bonds to four H atoms to form H_4O units, and there are four F atoms coordinated near each H_4O unit, which are almost on the extension line of the O-H bond. The O-H-F angle is nearly linear and varies from 160° to 170° in the pressure range of stability of this phase. In H_5OF_3, the relationship between F and H_4O units is similar to H_4OF_2. H_5OF_3 consists of three types of units, H_4O^{2+}, HF, and F^-. Thus, H_5OF_3 can be redefined as $H_4OF_2 \cdot HF$. The electron localization function (ELF) [35] was calculated to obtain further insight into the bonding patterns of these phases. Figures 2(c) and 2(d) show the ELF (isosurface at 0.75) of H_4OF_2 and $H_4OF_2 \cdot HF$, respectively, at 150 GPa, and clearly illustrate the presence of discrete molecular ions. High ELF (∼0.9) between O and H atoms in the H_4O unit indicates strong covalent bonds (O-H) in both structures, while there is no strong electronic localization between H_4O units and F atoms in H_4OF_2 or $H_4OF_2 \cdot HF$.

Figure 3 shows the variation of the H-O distance (in the H_4O unit) and the H-F distance (between the H_4O unit and

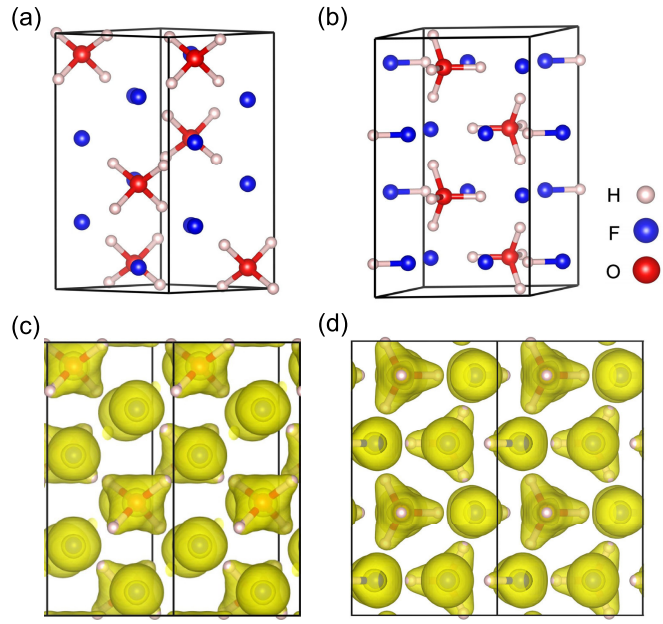

FIG. 2. Crystal structures and electronic localization function of H_4OF_2 and $H_4OF_2 \cdot HF$. [(a), (c)] H_4OF_2 in a $C2/c$ structure at 150 GPa. [(b), (d)] $H_4OF_2 \cdot HF$ in a $P2_1/m$ structure at 150 GPa. To clarify, a $1 \times 2 \times 1$ supercell was used to display the structure of $H_4OF_2 \cdot HF$ and the isosurface plots at ELF = 0.75.

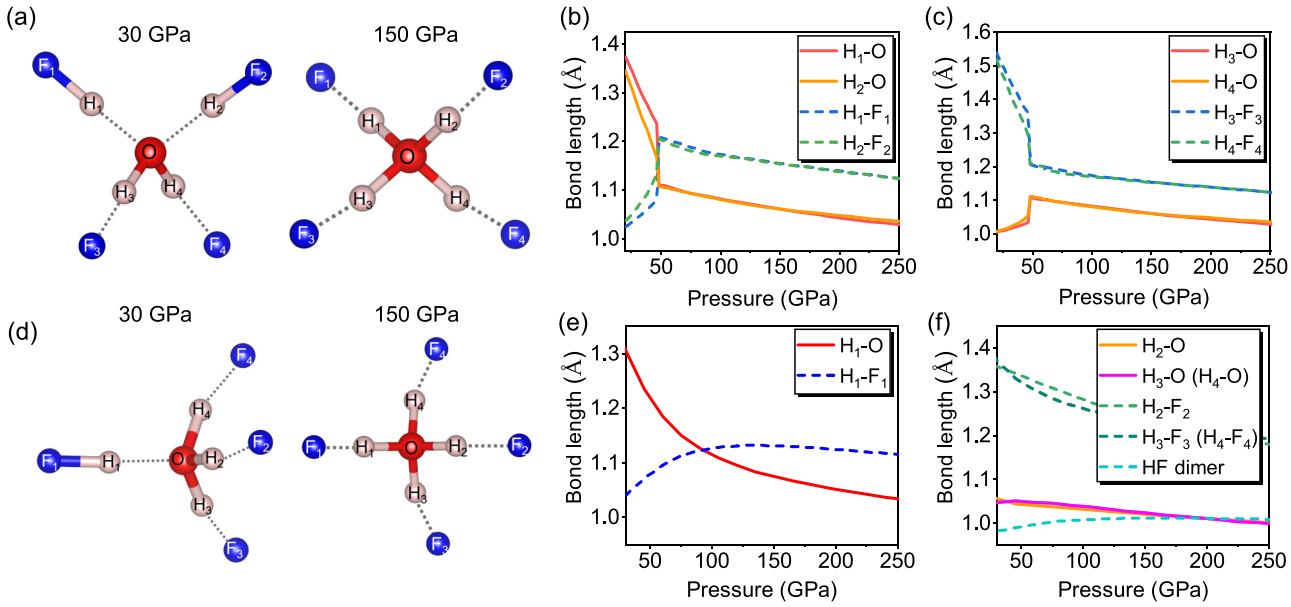

FIG. 3. Bond lengths as a function of pressure. Schematic representations of proton transfer in (a) H_4OF_2 and (d) $H_4OF_2 \cdot HF$ from 30 to 150 GPa. The evolution of the H-O distance within the H_4O unit and the H-F distance between the H_4O unit and F atoms in [(b), (c)] H_4OF_2 and [(e), (f)] $H_4OF_2 \cdot HF$ under pressure.

the coordinating F atoms) in these two compounds under pressure. The low-pressure structure of H_4OF_2, as depicted in Fig. 3(a), exhibits oxygen being surrounded by only two H atoms (labeled H_3 and H_4), representing the presence of H_2O molecules, while the atoms labeled H_1 and H_2 belong to the HF molecules. As pressure increases, there is a displacement of H_1 and H_2 away from fluorine atoms towards oxygen atoms. At approximately 50 GPa, an abrupt elongation of H-F bonds and shrinkage of H-O bonds occurs, resulting in all H-O bond lengths becoming shorter than the corresponding H-F bond lengths. This phenomenon indicates the protons transfer from the 2HF molecules to the H_2O molecules under pressure [Figs. 3(a)–3(c)]. However, in the $H_4OF_2 \cdot HF$ phase, the situation differs. At low pressure, the oxygen atom is surrounded by three hydrogen atoms representing the H_3O^+ ion (labeled as H_2, H_3, and H_4), while only the hydrogen atom labeled as H_1 belongs to the HF molecule. As pressure increases, only the bonds between H_1-O and H_1-F_1 exhibit abnormal changes. Specifically, proton transfer occurs from the HF molecule to the H_3O^+ molecular ion under pressure. Once the pressure exceeds 100 GPa, all of the H-O bonds become shorter than the H-F bond length (excluding the HF dimer) [Figs. 3(d)–3(f)]. After proton transfer is accomplished, all the O-H bonds (∼1.08 Å at 100 GPa) also turn out to be significantly shorter than the O-H bond length in ice X (∼1.15 Å at 100 GPa), and the H-F bonds (∼1.17 Å at 100 GPa) are longer than the H-F bond in the *Cmcm*-HF phase (∼1.09 Å at 100 GPa). The emergence of the H_4O unit is accompanied by intermolecular proton transfer driven by pressure.

To further clarify the nature of chemical bonds under pressure, we performed Bader topological analysis of electron density [36], which has been successfully applied to the determination of significant interactions through the values of the charge density and its Laplacian at bond critical points. A high value of electron density and its negative Laplacian indicate a covalent bond. Increasing density and decreasing Laplacians indicate that a covalent bond is getting stronger [28,36]. As shown in Fig. 4, $\nabla^2\rho_{(\text{H-O})}$ ($\rho_{(\text{H-O})}$) in two compounds share consistent (opposite) changes with bond length. $\nabla^2\rho_{(\text{H-O})}$ ($\rho_{(\text{H-O})}$) decrease (increase) with increasing pressure, which indicates the accumulation of charge, that is, the increase of covalence. $\nabla^2\rho_{(\text{H-F})}$ ($\rho_{(\text{H-F})}$) shows an opposite trend with pressure. Thus, the H-O bond in the H_4O unit has a highly negative value and is thus strongly covalent. In

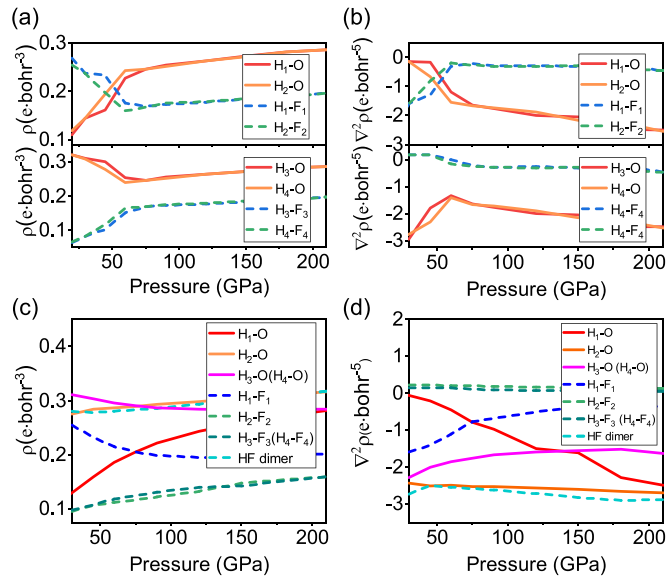

FIG. 4. Bond topological parameters as a function of pressure. The value of topological parameters of Bond critical points in [(a), (b)] H_4OF_2 and [(c), (d)] $H_4OF_2 \cdot HF$ as a function of pressure. ρ and $\nabla^2\rho$ are the charge density and its Laplacian at the corresponding bond critical points, respectively.

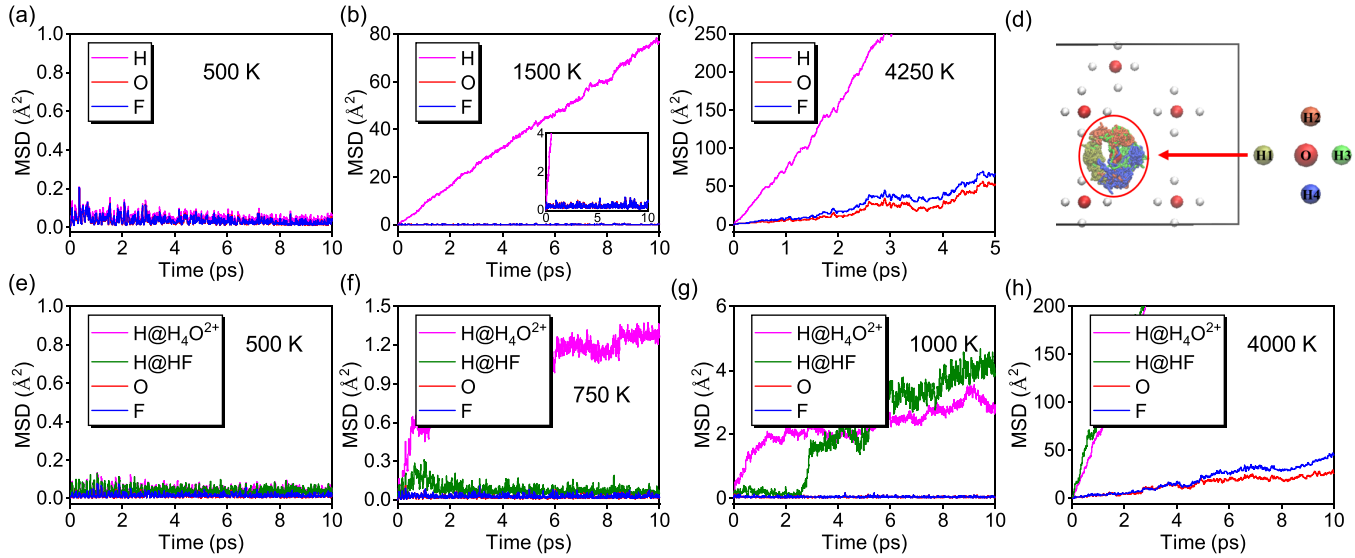

FIG. 5. Dynamical behavior of H_4OF_2 and $H_4OF_2 \cdot HF$ from AIMD simulations. Mean square displacements of the hydrogen, oxygen, and fluorine atoms in [(a)–(c)] H_4OF_2 (with a density of 3.77 g/cm^3) and [(e)–(h)] $H_4OF_2 \cdot HF$ (with a density of 4.03 g/cm^3) at selected temperatures. (d) The schematic of the atomic trajectories of $H@H_4O^{2+}$ in $H_4OF_2 \cdot HF$ phase at 750 K. The four hydrogen atoms in the H_4O unit are represented by different colors and the trajectories show free rotor behavior. For clarity we do not show the F atoms and the H@HF atoms, which only oscillate around their equilibrium positions.

comparison, the $\nabla^2\rho_{(\text{H-F})}$ values for the H-F bond are close to zero after the proton is transferred, showing ionic character. Combined with the large constant charge transfer between the H_4O unit and F atom (see Appendix D), it can be inferred that the H_4O^{2+} ion is stabilized by pressure. Specifically, for $H_4OF_2 \cdot HF$, both $\nabla^2\rho_{(\text{HFdimer})}$ and $\rho_{(\text{HFdimer})}$ indicate the presence of discrete HF molecular units, which exhibit a stronger covalent characteristic than H-O in the H_4O unit.

Note that pure H_2O and HF are known to show unique physical states at high temperatures and high pressures. H_2O has a superionic phase boundary over 1500 K, persisting in a very wide pressure range from about 50 GPa to several hundred GPa [23,37–41]. For pure HF, it has been reported that superionic state appears at 33 GPa at a temperature of 900 K [42]. We decided to investigate the dynamical properties of the predicted H_4O^{2+}-containing compounds at high temperatures further, and performed *ab initio* molecular dynamics (AIMD) simulations in the pressure range 70–250 GPa and temperatures in the range 0–5500 K. Each symbol in Fig. 6 represents an AIMD simulation, in which the state of matter is distinguished by analyzing mean square displacements (MSDs). Taking the simulation of H_4OF_2 (with a density of 3.77 g/cm^3) at 500 K as an example, the MSDs of hydrogen, oxygen, and fluorine quickly level off after the initial ballistic region and yield zero diffusion coefficients for all atoms, indicating the characteristics of a normal solid [Fig. 5(a)]; at 1500 K, hydrogen atoms start diffusing, whereas oxygen and fluorine atoms still oscillate around their equilibrium positions [Fig. 5(b)]. This is typical of the superionic state in which some atoms rapidly diffuse (here, only hydrogens possess nonzero diffusion constants) through the lattice of the remaining species, as was seen in water ice [23–27,37–41] and ammonia ice [23,43]. At 4250 K, all sublattices melt, exhibiting fluidlike diffusive behavior [Fig. 5(c)]. In the simulation of $H_4OF_2 \cdot HF$ (with a density of 4.03 g/cm^3), the results are similar to the H_4OF_2 phase at similar temperatures—normal state at 500 K [Fig. 5(e)], superionic state at 1000 K [Fig. 5(g)], and fluid state at 4000 K [Fig. 5(h)], respectively. However, in the transition region from normal to superionic state, there is a region where H_4O^{2+} enters a plastic state at 750 K. As shown in Figs. 5(f) and 5(d), the distribution of four hydrogen atoms around the oxygen atom overlaps due to the rotation of the H_4O unit. The H_4O^{2+} ion shows similar behavior to ice [40], ammonia [43], and methane [44] as a free rotor at certain *P*-*T* conditions, and thus truly behaves as a discrete molecular ion. Meanwhile, H@HF maintains solid-state behavior in the plastic state. The phase classification of all the compounds was confirmed by the calculations of diffusion coefficients compared to ice.

With such analysis, we established an approximate phase boundary between the different states of the H_2O-HF mixtures in Fig. 6. Differences in H, O, and F melting temperatures distinguish several regions in H_4OF_2 and there is an additional narrow region of plastic state in $H_4OF_2 \cdot HF$. Note that the melting curve calculated by direct heating may be overestimated due to the well-known overheating effect, and a more accurate evaluation requires calculating free energy at finite temperatures or using the two-phase approach. As shown in Fig. 6, the hydrogen diffusion temperatures in the H_2O-HF system are generally lower than those of water ice [23,37–41], indicating a weaker H-O interaction in H_4O^{2+}, although the H-O bonds in H_4O^{2+} are shorter than in H_2O. In $H_4OF_2 \cdot HF$, the phase boundary of the superionic state also shifts down significantly as the proportion of HF increases. The addition of acidic molecules (the injection of more protons) will cause hydrogen atoms to enter the superionic state at lower temperatures. A similar situation also occurs in ammonia-water mixtures [45–47].

To verify the thermal stability of aquodiium at high temperatures, we tracked the changes in the coordination number

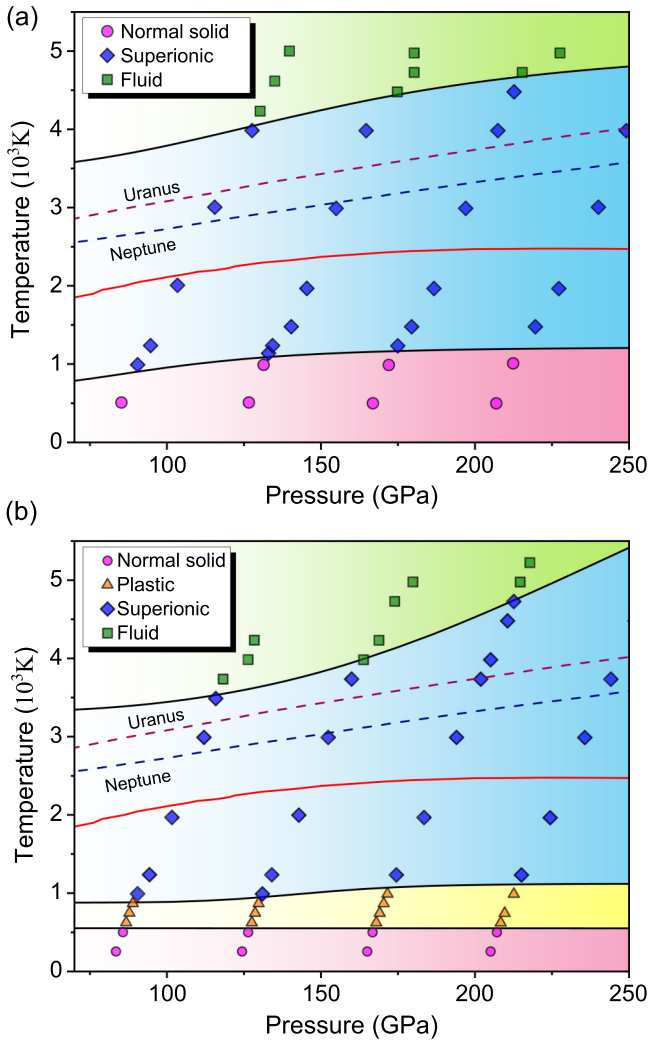

FIG. 6. Pressure-temperature phase diagram. Phase diagram of (a) H_4OF_2 and (b) $H_4OF_2 \cdot HF$. Circles, diamonds, and squares represent the normal solid state, superionic hydrogen state, and fluid state, respectively. In (b), triangles represent the plastic state. Phase boundaries between different states are distinguished by black solid lines and the isentropes for Uranus and Neptune [41,48] (dark purple and dark blue dashed lines) as well as the phase boundary between normal and superionic phases of water ice [41] (red solid line) are also shown.

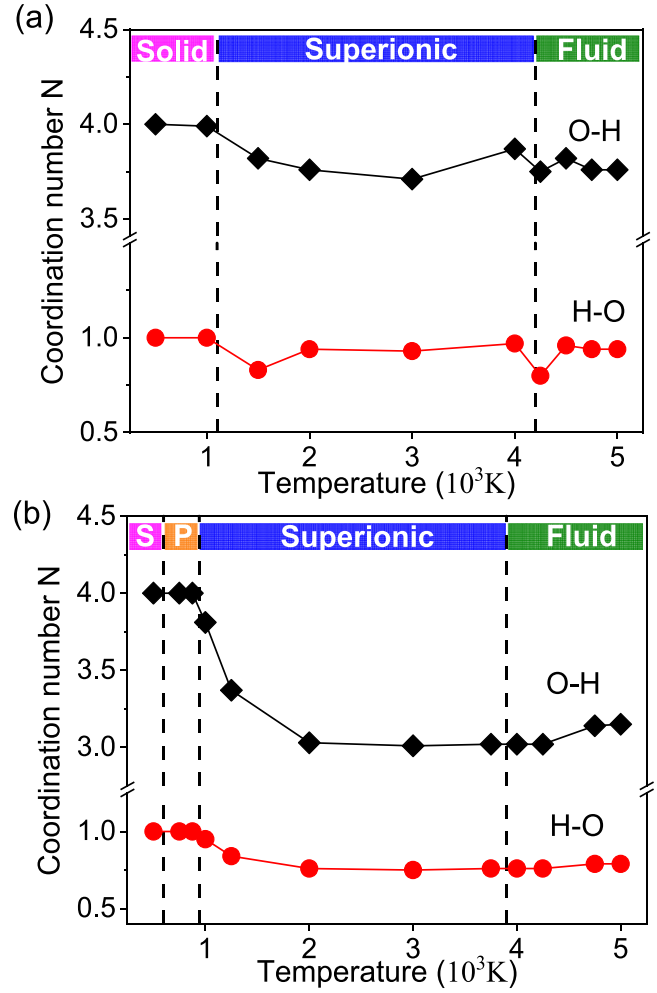

FIG. 7. The integrated coordination number for O-H (O is the central atom and H is the coordinating atom) and H-O (H is the central atom and O is the coordinating atom) of H_4O units in (a) H_4OF_2 and (b) $H_4OF_2 \cdot HF$ as a function of temperature. The coordination number N is defined as the integral of the radial distribution function $g(r)$ from zero to its first minimum. Approximate boundaries between different states are given by dashed lines.

of hydrogen (oxygen) around oxygen (hydrogen) for two structures in AIMD (Fig. 7). The N(O-H) and N(H-O) coordination numbers are equal to 4 and 1 below 1000 K, respectively, indicating H_4O^{2+} ions in both structures. At temperatures above 1000 K, N(O-H) [N(H-O)] begin to decrease and then converge to 3.75 (0.85) and 3.1 (0.8) for H_4OF_2 and $H_4OF_2 \cdot HF$, respectively (Fig. 7), implying that some of the H_4O^{2+} ions are destroyed at high temperatures. Specifically, in their superionic and fluid regions, most transient fragments in H_4OF_2 contain H_4O^{2+} species compared with the $H_4OF_2 \cdot HF$ phase. For H_4OF_2, its N(O-H) is above 3.5 even in its fluid state, so more than half of H_4O^{2+} cations persist even after the compound melts.

Given the high stability of aquodiium at high pressures and high temperatures, here we discuss two possible scenarios of its survival conditions. As shown in Fig. 6, the *P-T* boundary of the fluid is slightly higher than the isentropes of Uranus or Neptune [48]. The aquodiium may exist in acidic regions inside these icy giant planets and gives us an insight that some minor elements, such as F, can greatly change the behavior of proton transport and ice superionization, which would affect the magnetic field and matter cycle inside water-rich planets [49–51]. Interestingly, there is a natural antipode of aquodiium—the "hydrogarnet defect" [52–54] in some silicate garnets, well-known minerals. There, Si atoms inside tetrahedral ions $(SiO_4)^{4-}$ are removed, and the resulting charge of the vacancy (V_{Si}) is compensated by protonating all four of the surrounding oxygen atoms, forming four OH groups ($(OH^-)_4$). To further highlight the difference, the hydrogarnet defect appears in alkaline conditions, whereas $[H_4O]^{2+}$ corresponds to acidic conditions. It is conceivable that the aquodiium $[H_4O]^{2+}$ ion can also exist as a defect in silicate minerals formed in strongly acidic conditions.

At ambient pressure, many acids are much stronger than HF, such as HBr, and are more powerful protonating agents. This means that aquodiium ions could appear in other systems at lower pressures. However, for the HBr-H_2O system, this does not happen: our calculations show no stable compounds between H_2O and HBr at pressures up to 300 GPa. Pressure also seems to drastically affect the affinity to protons, just as it can change the electron affinities of the atoms [55]. Further research into the proton affinities at high pressure will be a significant contribution to the fundamentally important theory of acids and bases.

III. CONCLUSION

In summary, systematic searches in the H_2O-HF system yielded three stable compounds: H_3OF, H_4OF_2, and $H_4OF_2 \cdot HF$. As expected, in an acidic environment, the stable hydronium solid easily forms at low temperatures, and further increase of pressures forces H_3O^+ to overcome the repulsion from H^+, forming a new cation H_4O^{2+}, present in both H_4OF_2 and $H_4OF_2 \cdot HF$. Analysis of the proton transfer mechanism, topology of electron density distribution, and Bader charges confirm the existence of aquodiium in H_4OF_2 and $H_4OF_2 \cdot HF$. AIMD simulations and analysis of local coordination confirm that, even at very high temperatures (corresponding to superionic and fluid phases), most aquodiium ions are preserved. Pressure-induced emergence of aquodiium is fundamental for basic chemical theories such as the VSEPR model, proton transfer, and acid-base theory.

ACKNOWLEDGMENTS

This work was supported by NSFC (Grants No. 92263101, No. 12174200, No. 21803033, No. 52025026, No.11874224, and No. 52090020) and the 2020-JCJQ project (GFJQ2126-007). The calculations were performed at Tianhe II in Guangzhou and Supercomputing Center of Nankai University (NKSC). X.D. and X.F.Z. are thankful for the computing resources of Tianhe II and the support of the Chinese National Supercomputer Center in Guangzhou. A.R.O. acknowledges funding from the Russian Science Foundation (Grant No. 19–72–30043).

APPENDIX A: COMPUTATIONAL DETAILS

We used the variable-composition evolutionary algorithm USPEX [29,30] to search for the crystal structure, and variation operators such as heredity, lattice mutation, and transmutation were used to ensure the diversity of compositions and search efficiency. In the H_2O-HF system, extensive structure searches were severally performed at pressures of 50, 80, 100, 120, 150, 200, 300 GPa. Each search contained up to 40 atoms per primitive cell and ran for 60 generations with 80 structures in every generation and all structures were relaxed at given pressure and zero temperature. In addition, some lowest-enthalpy structures were further checked by fixed-composition evolutionary searches. The H-F-O structure searches at 80 and 150 GPa were subsequently executed and each search contained up to 40 atoms per primitive cell and ran for 30 generations with 120 structures in every generation.

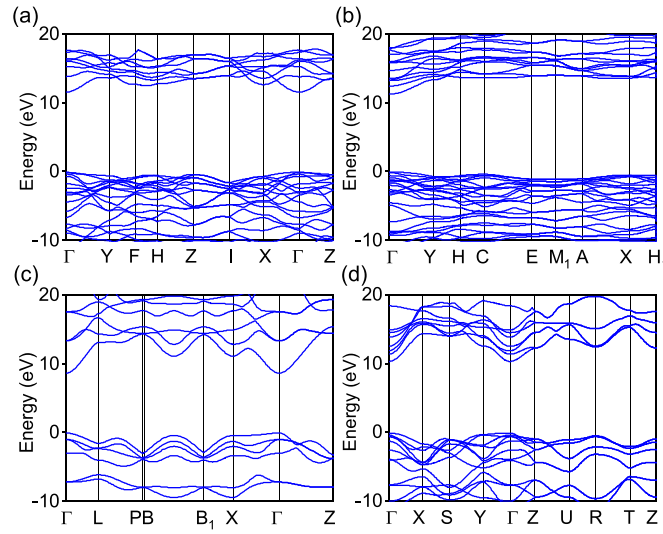

FIG. 8. Band structure of (a) $C2/c$ H_4OF_2 at 150 GPa, (b) $P2_1/m$ H_5OF_3 at 150 GPa, (c) $R3m$ H_3OF at 50 GPa, and (d) $Pmma$ H_3OF at 100 GPa. Their DFT band gaps under corresponding pressure are 11.64, 11.31, 8.69, and 10.40 eV, respectively, reflecting the properties of insulators.

First-principles total-energy and electronic property calculations were carried out using density functional theory as implemented in the VASP code [56], adopting the all-electron projector-augmented wave [57] methods with $1s$, $2s^2\,2p^4$, and $2s^2\,2p^5$ treated as valence electrons for H, O, and F, respectively. In addition, the cutoff radii were chosen no greater than 1.4 bohrs for oxygen and fluorine, and 0.7 bohr for hydrogen. The generalized gradient approximation with the functional of Perdew, Burke, and Ernzerhof [58] was adopted to treat the exchange-correlation energy. A cutoff energy of 1350 eV for the plane-wave expansion and fine Monkhorst-Pack k meshes of $2\pi \times 0.03$ Å^{-1} were chosen to ensure energy and force convergences better than 10^{-7} eV and 10^{-3} eV/Å.

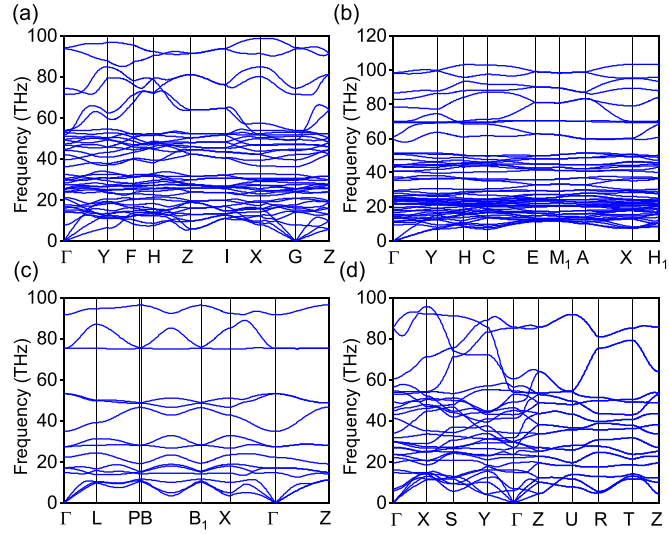

FIG. 9. Phonon dispersion curves of (a) $C2/c$ H_4OF_2 at 150 GPa, (b) $P2_1/m$ H_5OF_3 at 150 GPa, (c) $R3m$ H_3OF at 50 GPa, and (d) $Pmma$ H_3OF at 100 GPa.

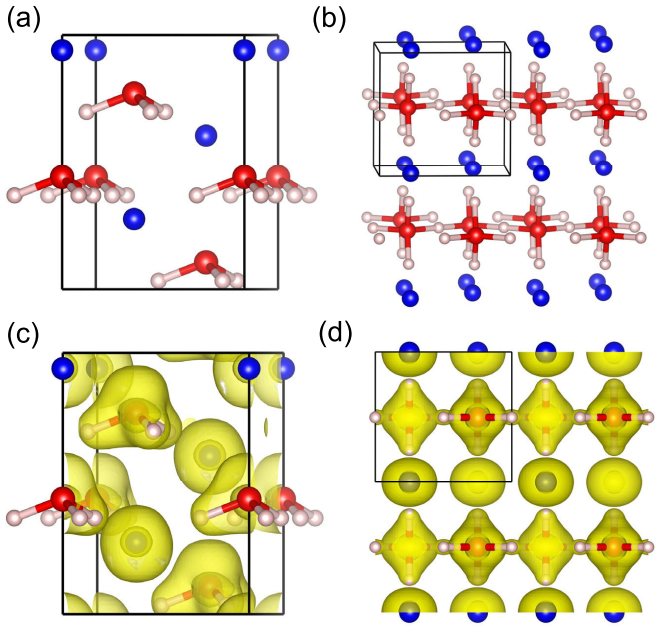

FIG. 10. Crystal structures and ELF isosurfaces for [(a), (c)] *R*3*m* H_3OF at 50 GPa and [(b), (d)] *Pmma* H_3OF at 100 GPa. For clarity, a $2 \times 2 \times 1$ supercell was used to display the layered characteristics of *Pmma* H_3OF and the ELF isosurface plots at 0.75.

Quasiharmonic free-energy calculations and phonon dispersion curves were computed using the PHONOPY [59] code.

AIMD simulations, implemented in VASP, were performed at selected pressure with temperatures ranging from 500 to 6000 K. We used a simulation unit with 252 atoms for *C*2/*c* H_4OF_2 and 144 atoms for $P2_1/m$ $H_4OF_2 \cdot HF$, respectively. A Γ-centered *k*-point grid and cutoff energy of 1000 eV were used to ensure energy convergence of better than 10^{-6} eV. The canonical *NVT* ensemble was adopted with a Nosé-Hoover thermostat [60], lasting for 10 ps (5–20 ps) with a time step of 1 fs (0.5 fs) with temperatures below (higher than) 3000 K. Data after the simulation reached equilibrium were extracted to calculate averaged MSDs and integrated coordination number (*N*).

A Bader analysis algorithm [61] and bond topological analysis were utilized by dealing with the total charge density of the structure. All of these are based on the quantum theory of atoms in molecules [36]. In this theory, the charge density distribution $\rho(r)$ and its principal curvatures (the three eigenvalues of the Hessian matrix) at the bond critical point (BCP) reveal information about the type and properties of the bond. The sign of the second derivative of the electron density (Laplacian) value $[\nabla^2\rho(r)]$ at the BCP indicates concentration (negative) or depletion (positive) of electron density.

The drawing of the crystal structure and ELF isosurfaces were created using VESTA [62] software.

APPENDIX B: CRYSTAL STRUCTURE INFORMATION, ELECTRON BAND STRUCTURE, AND PHONON DISPERSION CURVE OF THE PREDICTED PHASE

In this appendix, we provide the crystal structure information, electron band structure, and phonon dispersion curves for H_3OF, H_4OF_2 and H_5OF_3 as shown in Table I, Fig. 8, and Fig. 9, respectively.

TABLE II. Bader charges for *R*3*m* (50 GPa) and *Pmma* (100 GPa) phases of H_3OF.

	Atom	*R*3*m*		*Pmma*	
		Charge ($\|e\|$)	δ ($\|e\|$)	Charge ($\|e\|$)	δ ($\|e\|$)
H_3O^{δ}	O1	−1.121	+0.690	−1.273	+0.746
	H1	+0.597		+0.681	
	H2	+0.605		+0.681	
	H3	+0.610		+0.657	
F^{δ}	F1	−0.690	−0.690	−0.746	−0.746

TABLE III. Bader charges in H_4OF_2 and $H_4OF_2 \cdot HF$ at selected pressures.

	Atom charge ($\|e\|$)	Pressure (GPa)		
		100	200	300
*C*2/*c* H_4OF_2	H1	+0.680	+0.695	+0.699
	H2	+0.680	+0.695	+0.699
	H3	+0.692	+0.701	+0.700
	H4	+0.692	+0.701	+0.700
	O	−1.262	−1.294	−1.299
	F1	−0.739	−0.748	−0.748
	F2	−0.745	−0.750	−0.751
	H_4O	+1.484	+1.498	+1.500
	F	−0.742	−0.749	−0.750
$P2_1/m$ $H_4OF_2 \cdot HF$	H1	+0.694	+0.705	+0.692
	H2	+0.707	+0.714	+0.696
	H3	+0.697	+0.701	+0.653
	H4	+0.697	+0.701	+0.653
	H5(H@HF)	+0.732	+0.732	+0.698
	O	−1.269	−1.296	−1.202
	F1	−0.748	−0.745	−0.720
	F2	−0.733	−0.736	−0.721
	F3(F@HF)	−0.777	−0.776	−0.749
	H_4O	+1.526	+1.526	+1.492
	F	−0.741	−0.741	−0.721
	HF dimer	−0.045	−0.044	−0.052

APPENDIX C: CRYSTAL STRUCTURES, ELECTRON LOCALIZATION FUNCTION, AND CHARGE TRANSFER OF THE H_3OF COMPOUND

The H_3OF compound has two phases. The *R*3*m* phase consists of H_3O and F units (Fig. 10), and charge transfer reflects that this is a molecular ionic phase (Table II). As pressure increases, the *R*3*m* phase transforms into the *Pmma* phase [Fig. 1(c)], where neighboring H_2O units share one H atom to form a zigzag chain of H-sharing H_3O units. In this structure, layers of F^- ions alternate with chains of H_3O^+ ions (Fig. 10). The bridging O-H bond length is 1.137 Å and the apical O-H bond length is 1.056 Å, shorter than the O-H bond length in ice X (*Pn*-3m). The H-F bond length in the stacking direction is 1.193 Å and greater than the H-F bond

length in *Cmcm* HF. There is a large charge transfer between the coupled layers (Table II).

APPENDIX D: CHARGE TRANSFER OF H_4OF_2 AND H_5OF_3

Table III shows Bader charges in two compounds at selected pressures. The charge transfer is almost pressure independent, resulting in approximately +1.5 charges for H_4O^{2+} ions and −0.75 for F^- ions, while the HF molecules remain nearly neutral. It should be noted that Bader charges are usually notably smaller than the formal oxidation numbers, even for typical ionic crystals such as CsF (0.81 at 100 GPa), let alone for covalent or molecular compounds [10]. The large constant charge transfer after the formation of the H_4O unit reinforces that H_4O^{2+} ions are well-defined units in H_4OF_2 and $H_4OF_2 \cdot HF$.

[1] W. Koch, N. Heinrich, H. Schwarz, F. Maquin, and D. Stahl, Combined experimental and ab initio molecular orbital studies on gaseous OH_n^{2+} species ($n = 1 - 4$), Int. J. Mass Spectrom. Ion Processes **67**, 305 (1985).

[2] G. A. Olah, G. K. Prakash, M. Barzaghi, K. Lammertsma, P. V. R. Schlyer, and J. A. Pople, Protonated hydronium dication, H4O2+. Hydrogen-deuterium exchange of D*d*2H17O+ in HF:SbF5 and DH217O+ in DF:SbF5 and theoretical calculations, J. Am. Chem. Soc. **108**, 1032 (1986).

[3] H. Schmidbaur, S. Hofreiter, and M. Paul, Synthesis of the gold analogue of the elusive doubly protonated water molecule, Nature (London) **377**, 503 (1995).

[4] R. J. Gillespie and I. Hargittai, *The VSEPR Model of Molecular Geometry* (Dover, New York, 2012).

[5] N. Hartz, G. Rasul, and G. A. Olah, Chemistry in superacids. 10. Role of oxonium, sulfonium, and carboxonium dications in superacid-catalyzed reactions, J. Am. Chem. Soc. **115**, 1277 (1993).

[6] V. P. Reddy, E. Sinn, G. A. Olah, G. K. S. Prakash, and G. Rasul, Theoretical investigation of superelectrophilic fluorooxonium dications FOH_3^{2+} and $F_2OH_2^{2+}$: Comparison with parent H_4O^{2+} dication, J. Phys. Chem. A **108**, 4036 (2004).

[7] L. Zhang, Y. Wang, J. Lv, and Y. Ma, Materials discovery at high pressures, Nat. Rev. Mater. **2**, 17005 (2017).

[8] M. Miao, Y. Sun, E. Zurek, and H. Lin, Chemistry under high pressure, Nat. Rev. Chem. **4**, 508 (2020).

[9] W. Zhang, A. R. Oganov, A. F. Goncharov, Q. Zhu, S. E. Boulfelfel, A. O. Lyakhov, E. Stavrou, M. Somayazulu, V. B. Prakapenka, and Z. Konôpková, Unexpected stable stoichiometries of sodium chlorides, Science **342**, 1502 (2013).

[10] M. Miao, Caesium in high oxidation states and as a *p*-block element, Nat. Chem. **5**, 846 (2013).

[11] Q. Zhu, A. R. Oganov, and Q. Zeng, Formation of stoichiometric CsF_n compounds, Sci. Rep. **5**, 7875 (2015).

[12] Q. Zhu, D. Y. Jung, A. R. Oganov, C. W. Glass, C. Gatti, and A. O. Lyakhov, Stability of xenon oxides at high pressures, Nat. Chem. **5**, 61 (2012).

[13] L. Zhu, H. Liu, C. J. Pickard, G. Zou, and Y. Ma, Reactions of xenon with iron and nickel are predicted in the Earth's inner core, Nat. Chem. **6**, 644 (2014).

[14] X. Dong, A. R. Oganov, A. F. Goncharov, E. Stavrou, S. Lobanov, G. Saleh, G.-R. Qian, Q. Zhu, C. Gatti, V. L. Deringer, R. Dronskowski, X.-F. Zhou, V. B. Prakapenka, Z. Konôpková, I. A. Popov, A. I. Boldyrev, and H.-T. Wang, A stable compound of helium and sodium at high pressure, Nat. Chem. **9**, 440 (2017).

[15] J. Zhang, J. Lv, H. Li, X. Feng, C. Lu, S. A. T. Redfern, H. Liu, C. Chen, and Y. Ma, Rare helium-bearing compound FeO_2He stabilized at deep-earth conditions, Phys. Rev. Lett. **121**, 255703 (2018).

[16] Z. Liu, J. Botana, A. Hermann, S. Valdez, E. Zurek, D. Yang, H.-q. Lin, and M.-s. Miao, Reactivity of He with ionic compounds under high pressure, Nat. Commun. **9**, 951 (2018).

[17] C. Liu, H. Gao, Y. Wang, R. J. Needs, C. J. Pickard, J. Sun, H.-T. Wang, and D. Xing, Multiple superionic states in helium–water compounds, Nat. Phys. **15**, 1065 (2019).

[18] A. Polian and M. Grimsditch, New high-pressure phase of H_2O: Ice X, Phys. Rev. Lett. **52**, 1312 (1984).

[19] R. J. Hemley, A. P. Jephcoat, H. K. Mao, C. S. Zha, L. W. Finger, and D. E. Cox, Static compression of H_2O-ice to 128 GPa (1.28 Mbar), Nature (London) **330**, 737 (1987).

[20] V. F. Petrenko and R. W. Whitworth, *Physics of Ice* (Oxford University Press, Oxford, 1999).

[21] B. Militzer and H. F. Wilson, New phases of water ice predicted at megabar pressures, Phys. Rev. Lett. **105**, 195701 (2010).

[22] C. J. Pickard, M. Martinez-Canales, and R. J. Needs, Decomposition and terapascal phases of water ice, Phys. Rev. Lett. **110**, 245701 (2013).

[23] C. Cavazzoni, G. L. Chiarotti, S. Scandolo, E. Tosatti, M. Bernasconi, and M. Parrinello, Superionic and metallic states of water and ammonia at giant planet conditions, Science **283**, 44 (1999).

[24] M. French, T. R. Mattsson, N. Nettelmann, and R. Redmer, Equation of state and phase diagram of water at ultrahigh pressures as in planetary interiors, Phys. Rev. B **79**, 054107 (2009).

[25] M. French, T. R. Mattsson, and R. Redmer, Diffusion and electrical conductivity in water at ultrahigh pressures, Phys. Rev. B **82**, 174108 (2010).

[26] E. Sugimura, T. Komabayashi, K. Ohta, K. Hirose, Y. Ohishi, and L. S. Dubrovinsky, Experimental evidence of superionic conduction in H_2O ice, J. Chem. Phys. **137**, 194505 (2012).

[27] M. Millot, F. Coppari, J. R. Rygg, A. C. Barrios, S. Hamel, D. C. Swift, and J. H. Eggert, Nanosecond x-ray diffraction of shock-compressed superionic water ice, Nature (London) **569**, 251 (2019).

[28] Y. Wang, H. Liu, J. Lv, L. Zhu, H. Wang, and Y. Ma, High pressure partially ionic phase of water ice, Nat. Commun. **2**, 563 (2011).

[29] A. R. Oganov and C. W. Glass, Crystal structure prediction using ab initio evolutionary techniques: Principles and applications, J. Chem. Phys. **124**, 244704 (2006).

[30] A. O. Lyakhov, A. R. Oganov, H. T. Stokes, and Q. Zhu, New developments in evolutionary structure prediction algorithm USPEX, Comput. Phys. Commun. **184**, 1172 (2013).

[31] J. M. Besson, Ph. Pruzan, S. Klotz, G. Hamel, B. Silvi, R. J. Nelmes, J. S. Loveday, R. M. Wilson, and S. Hull, Variation of

interatomic distances in ice VIII to 10 GPa, Phys. Rev. B **49**, 12540 (1994).
[32] A. J. Leadbetter, R. C. Ward, J. W. Clark, P. A. Tucker, T. Matsuo, and H. Suga, The equilibrium low-temperature structure of ice, J. Chem. Phys. **82**, 424 (1985).
[33] M. W. Johnson, E. Sandor, and E. Arzi, The crystal structure of deuterium fluoride, Acta Crystallogr. Sect. B: Struct. Crystallogr. Cryst. Chem. **31**, 1998 (1975).
[34] L. Zhang, Y. Wang, X. Zhang, and Y. Ma, High-pressure phase transitions of solid HF, HCl, and HBr: An *ab initio* evolutionary study, Phys. Rev. B **82**, 014108 (2010).
[35] A. Savin, R. Nesper, S. Wengert, and T. F. Fässler, ELF: The electron localization function, Angew. Chem. Int. Ed. Engl. **36**, 1808 (1997).
[36] R. F. W. Bader, *Atoms in Molecules: A Quantum Theory* (Oxford University Press, Oxford, 1994).
[37] R. Redmer, T. R. Mattsson, N. Nettelmann, and M. French, The phase diagram of water and the magnetic fields of Uranus and Neptune, Icarus **211**, 798 (2011).
[38] H. F. Wilson, M. L. Wong, and B. Militzer, Superionic to superionic phase change in water: Consequences for the interiors of Uranus and Neptune, Phys. Rev. Lett. **110**, 151102 (2013).
[39] J. Sun, B. K. Clark, S. Torquato, and R. Car, The phase diagram of high-pressure superionic ice, Nat. Commun. **6**, 8156 (2015).
[40] J.-A. Hernandez and R. Caracas, Proton dynamics and the phase diagram of dense water ice, J. Chem. Phys. **148**, 214501 (2018).
[41] B. Cheng, M. Bethkenhagen, C. J. Pickard, and S. Hamel, Phase behaviours of superionic water at planetary conditions, Nat. Phys. **17**, 1228 (2021).
[42] N. Goldman and L. E. Fried, First principles simulation of a superionic phase of hydrogen fluoride (HF) at high pressures and temperatures, J. Chem. Phys. **125**, 044501 (2006).
[43] S. Ninet, F. Datchi, and A. M. Saitta, Proton disorder and superionicity in hot dense ammonia ice, Phys. Rev. Lett. **108**, 165702 (2012).
[44] L. Spanu, D. Donadio, D. Hohl, and G. Galli, Theoretical investigation of methane under pressure, J. Chem. Phys. **130**, 164520 (2009).
[45] V. N. Robinson and A. Hermann, Plastic and superionic phases in ammonia–water mixtures at high pressures and temperatures, J. Phys.: Condens. Matter **32**, 184004 (2020).
[46] M. Bethkenhagen, D. Cebulla, R. Redmer, and S. Hamel, Superionic phases of the 1:1 water-ammonia mixture, J. Phys. Chem. A **119**, 10582 (2015).
[47] X. Jiang, X. Wu, Z. Zheng, Y. Huang, and J. Zhao, Ionic and superionic phases in ammonia dihydrate $NH_3 \cdot 2H_2O$ under high pressure, Phys. Rev. B **95**, 144104 (2017).
[48] L. Scheibe, N. Nettelmann, and R. Redmer, Thermal evolution of Uranus and Neptune, Astron. Astrophys. **632**, A70 (2019).
[49] A. S. Naumova, S. V. Lepeshkin, P. V. Bushlanov, and A. R. Oganov, Unusual chemistry of the C–H–N–O system under pressure and implications for giant planets, J. Phys. Chem. A **125**, 3936 (2021).
[50] M. Hou *et al.*, Superionic iron oxide–hydroxide in Earth's deep mantle, Nat. Geosci. **14**, 174 (2021).
[51] H. Gao, C. Liu, J. Shi, S. Pan, T. Huang, X. Lu, H.-T. Wang, D. Xing, and J. Sun, Superionic silica-water and silica-hydrogen compounds in the deep interiors of Uranus and Neptune, Phys. Rev. Lett. **128**, 035702 (2022).
[52] C. Cohen-Addad, P. Ducros, and E. F. Bertaut, Étude de la substitution du groupement SiO_4 par $(OH)_4$ dans les composés $Al_2Ca_3(OH)_{12}$ et $Al_2Ca_3(SiO_4)_{2,16}$ $(OH)_{3,36}$ de type grenat, Acta Cryst. **23**, 220 (1967).
[53] J. Purton, R. Jones, M. Heggie, S. Öberg, and C. R. A. Catlow, LDF pseudopotential calculations of the α-quartz structure and hydrogarnet defect, Phys. Chem. Minerals **18**, 389 (1992).
[54] F. Pascale, P. Ugliengo, B. Civalleri, R. Orlando, P. D'Arco, and R. Dovesi, Hydrogarnet defect in chabazite and sodalite zeolites: A periodic Hartree-Fock and B3-LYP study, J. Chem. Phys. **117**, 5337 (2002).
[55] X. Dong, A. R. Oganov, H. Cui, X. F. Zhou, and H. T. Wang, Electronegativity and chemical hardness of elements under pressure, Proc. Natl. Acad. Sci. USA **119**, e2117416119 (2022).
[56] G. Kresse and J. Furthmüller, Efficient iterative schemes for *ab initio* total-energy calculations using a plane-wave basis set, Phys. Rev. B **54**, 11169 (1996).
[57] P. E. Blöchl, Projector augmented-wave method, Phys. Rev. B **50**, 17953 (1994).
[58] J. P. Perdew, K. Burke, and M. Ernzerhof, Generalized gradient approximation made simple, Phys. Rev. Lett. **77**, 3865 (1996).
[59] A. Togo and I. Tanaka, First principles phonon calculations in materials science, Scr. Mater. **108**, 1 (2015).
[60] W. G. Hoover, Canonical dynamics: Equilibrium phase-space distributions, Phys. Rev. A **31**, 1695 (1985).
[61] W. Tang, E. Sanville, and G. Henkelman, A grid-based Bader analysis algorithm without lattice bias, J. Phys. Condens. Matter **21**, 084204 (2009).
[62] K. Momma and F. Izumi, VESTA 3 for three-dimensional visualization of crystal, volumetric and morphology data, J. Appl. Crystallogr. **44**, 1272 (2011).